Synergistic reduction of U(VI) and selective oxidation of benzyl alcohol to prepare benzaldehyde via WO$_x$/g-C$_3$N$_4$

Feng He [a,b], Qianxiang Xiao [b], Yin Chen [b], Hongqing Wang [b,*], Xiangke Wang [c]

[a] School of Nuclear Science and Technology, University of South China, Hengyang, Hunan 421001, China
[b] Hunan Key Laboratory for the Design and Application of Actinide Complexes, School of Chemistry and Chemical Engineering, University of South China, Hengyang, Hunan 421001, China
[c] College of Environmental Science and Engineering, North China Electric Power University, Beijing 102206, China

ABSTRACT

In the photoreduction of U(VI), protective gases and additional sacrificial agents are still the major obstacles. Herein, we developed an oxygen-deficient WO$_x$/g-C$_3$N$_4$ catalyst for the simultaneous reduction of U(VI) and preparation of benzaldehyde by selective oxidation of benzyl alcohol without protective gases and sacrificial agents. The removal of U(VI) by WO$_x$/g-C$_3$N$_4$ could reach 98.5% and the conversion of benzyl alcohol was nearly 32% with a selectivity close to 100%. Compared with single g-C$_3$N$_4$ and defect-free WO$_3$, the photoreduction activity of WO$_x$/g-C$_3$N$_4$ was 10.4 and 7 times higher, respectively. Besides, the role of oxygen and oxygen defects was explored. Owing to oxygen defects in the catalyst, oxygen was adsorbed on the oxidation end (WO$_x$) of the catalyst and activated without entering the reduction end to interfere with the photoreduction of U(VI), while favoring the generation of •O$_2^-$ to improve the selectivity of benzaldehyde. Finally, a new mechanism was proposed.

1. Introduction

Due to uranium's chemical and radioactive toxicity, the emission of uranium-containing effluent poses a serious threat to the ecosystem and public health. Nowadays, the removal of uranium contaminants has become an urgent and critical issue [1–3]. Reducing solvable U(VI) to unsolvable U(IV) is a promising strategy for addressing uranium pollutants in terms of environmental protection [4,5]. Photocatalytic technology is regarded as an ideal solution for the conversion of U(VI) to U(IV) due to its natural richness of solar power, high efficiency, and sustainability [6,7]. In recent years, photocatalytic reduction of U(VI) has been reported extensively in the literature. Most of these studies concentrated on the modification of catalysts to increase the separation of photoinduced e$^-$-h$^+$ pairs, including elemental doping [8], heterojunction construction [9], and defect engineering [10], thereby enhancing photocatalytic activity. Nevertheless, some pervasive problems remain to be addressed. Two of the most prominent obstacles are that protective gases and additional sacrificial agents (generally organic matters) are generally essential in many photocatalytic systems [11,12].

The importance of protective gases is mainly related to the fact that oxygen in the photocatalytic system hinders the photocatalytic

reduction of uranyl, e.g., Wu et al. [13] reported that the P-introduced g-C$_3$N$_4$ photocatalytic reduction of uranyl was 74% higher under N$_2$ conditions than under oxygen conditions. Le et al. [14] used heterogeneous g-C$_3$N$_4$ for photoreduction of uranyl, and the reduction rate decreased by 51% under ambient air compared to that under a protective atmosphere. However, the protective atmosphere increases the difficulty of practical operation. In order to solve the problem of oxygen, scientists have explored different tactics. For example, Li et al. [15] realized uranyl reduction under moderate oxygen conditions by exploiting a strategy of requiring oxygen to participate in oxidation on the oxidation side to avoid oxygen entering the reduction side. Zhang et al. [16] utilized the interaction between oxygen and catalyst to sacrifice the catalyst to reduce the competition between oxygen and photoelectrons, achieving effective reduction of U(VI). Li et al. [17] successfully immobilized uranium by converting oxygen to an intermediate (H$_2$O$_2$) that was favorable for uranium immobilization. But, to our knowledge, at present, there are still no reports on eliminating the obstruction of oxygen to U(VI) reduction by designing catalyst structures that prevent oxygen from entering the reducing end without damaging the catalyst.

In addition, in U(VI) photoreduction systems, additional sacrificial

agents are generally required to eliminate h^+ in order to boost the separation ability of e^- and h^+. However, the sacrificial agents are usually oxidized to CO_2 and H_2O, which results in waste and undoubtedly increases economic costs. Even though there are still a few reports of efficient reduction of uranium without sacrificial agents, severe photocorrosion limits its practical application [16,18]. In our previous study [15], we have tried to reduce U(VI) at the reducing end while selectively oxidizing benzyl alcohol (BA) at the oxidizing end to prepare high value benzaldehyde (BD). Regrettably, BA was over-oxidized at the same time as the U(VI) reduction. So, is it possible to achieve selective oxidation of benzyl alcohol while simultaneously addressing the oxygen hindrance to U(VI) reduction?

Some studies have found that defects in oxygen-deficient catalysts promote oxygen adsorption and activation, thereby accelerating the oxidation of organics. For example, Zhao et al. [19] reported oxygen-deficient Cu/MnO_x nanosheets, which enhanced the adsorption and activation of molecular oxygen and hence leading to promote toluene oxidation. More interestingly, Zhang and colleagues [20] claimed that the introduction of oxygen vacancies on Au-BiOCl microsphere could supply abundant unsaturated sites for oxygen adsorption and promote the selective conversion of BA to BD. In addition, oxygen defect engineering is an effective means of tuning the energy band structure of metal-based oxides [10]. Whereas the energy band structure determines the reactive oxygen species, which is essential for selective oxidation of BA [21]. Based on the foregoing discussions, the introduction of oxygen defect engineering can not only increase oxygen adsorption and activation, but also adjust the catalyst energy band structure to control the generation of reactive oxygen species. Therefore, it is possible to immobilize oxygen at the oxidizing end without interfering with the reduction of U(VI) while realizing the selective oxidation of BA for BD preparation by rational catalyst structure design.

Among these photocatalysts, tungsten oxide (WO_3), an excellent photocatalyst, has been widely applied for organic pollutants degradation and oxygen evolution [22]. Defect regulation not only reduces the band gap of WO_3 and expands its light absorption range [23,24], but also boosts the oxidation of its oxidation end. However, due to poor carrier separation ability, the photocatalytic activity of WO_3 obtained through single defect regulation is still restricted. Fortunately, a heterojunction formed by two band-matched semiconductors can effectively overcome this issue. Additionally, the formation of composites allows oxidation and reduction reactions to take place on different component surfaces, which is also more conducive to immobilizing oxygen at the oxidizing end and avoiding interfering with the reduction of uranium. In addition, $g-C_3N_4$, a conjugated polymer semiconductor, is frequently employed in environmental remediation and the transformation of solar power [25,26]. Thanks to its strong physicochemical stability and suitable band gap (2.7 eV) [27], it could couple with a wide range of semiconductors (such as TiO_2 [28], WO_3 [29], and CdS [30]) to form heterojunctions.

Taking these above into consideration, $WO_x/g-C_3N_4$ composite was fabricated in this study. In the existence of oxygen, the material was highly efficient in reducing uranyl while selectively oxidizing BA to BD. More crucially, the reusability and anti-interference capability of $WO_x/g-C_3N_4$ proved its great potential for practical application.

2. Experimental

2.1. Chemicals

Urea (CH_4N_2O, ≥99%, AR), sodium tungstate dihydrate ($Na_2WO_4·2 H_2O$, 99.99%, AR), glucose monohydrate ($C_6H_{12}O_6·H_2O$, 98%, AR), citric acid ($C_6H_8O_7·H_2O$, 99.5%, AR), benzyl alcohol (BA, ≥99%, AR) and benzaldehyde (BD, ≥99%, AR) were purchased from Aladdin. Uranyl nitrate hexahydrate ($UO_2(NO_3)_2·6 H_2O$, ≥ 99%, AR) was acquired from Macklin. Anhydrous ethanol (EtOH, AR) and hydrochloric acid (HCl, 36–38%, AR) were obtained from Sinopharm Chemical

Reagent Co., Ltd. All the reagents used were analytical level.

2.2. Preparation of catalysts

$g-C_3N_4$ was obtained by the polycondensation of urea. Typically, 5.00 g of urea was heated to 550 °C in a muffle furnace at a rising rate of 5 °C/min under air circumstances, and then calcined for 4 h. The resulting products were allowed to recede to room temperature before being processed into powder.

To prepare WO_x and WO_3, 0.66 g $Na_2WO_4·2 H_2O$ was mixed with 60 mL deionized water, followed by 0.63 g citric acid monohydrate ($C_6H_8O_7·H_2O$) and 1.98 g glucose monohydrate ($C_6H_{12}O_6·H_2O$). After 20 min of vigorous stirring, 6 mL of hydrochloric acid (6 M) was added dropwise and rapidly stirred for half an hour. Afterwards, the suspension was removed into a 100 mL autoclave and kept at 120 ℃ for 24 h. After natural cooling to room temperature, the insoluble material was rinsed numerous times with anhydrous ethanol and deionized water alternately. Then, the sediment was put in a freeze dryer overnight. Finally, it was heated to 500 ℃ for 2 h in a tube furnace under an N_2 atmosphere to obtain WO_x, and the same procedure was employed to obtain WO_3 in an air environment.

The $WO_x/g-C_3N_4$ composite was fabricated in the following steps: 15 mg WO_x and 300 mg $g-C_3N_4$ were put into 30 mL of deionized water sequentially and vibrated ultrasonically until completely dispersed. The suspension was then filtered and desiccated in a freeze dryer for 12 h. Finally, the complexes were annealed at 300 ℃ for 2 h in N_2 to obtain oxygen deficient $WO_x/g-C_3N_4$ composite, while defect free $WO_3/g-C_3N_4$ composite was obtained via the same way under an air atmosphere.

2.3. Characterization

The crystallographic properties (XRD) were acquired from a Rigaku Ultima IV X-ray diffraction instrument (Japan) loaded with Cu Kα radiation at a scan speed of 2°/min. FI-IR spectra were analyzed by a Bruker Vertex7 infrared spectrometer (Germany). SEM images were collected using Zeiss Sigma 300 (Germany). XPS spectra were obtained from a Thermo Scientific ESCALAB Xi^+ (America) fitted with an Al Kα source (1486.68 eV) and calibrated with C1s (284.8 eV). UV–vis–DRS were measured by a Hitachi U-3900 spectrometer (Japan). TEM images were captured on a JEOL JEM-2100 F microscope (Japan) at an accelerating voltage of 100 kV. PL spectra were performed on an Edinburgh FLS1000 fluorescence spectrometer (England) with an excitation wavelength of 370 nm. ESR analyses were investigated on a Bruker A300 spectrometer (Germany) equipped with a 300 W Xe lamp. All the electrochemical measurements for this work were carried out on a CHI660e electrochemical workstation (China) furnished with a tri-electrode system in an electrolytic solution of 0.1 M Na_2SO_4 (except for linear sweep voltammetry curves). HPLC of organic components was recorded on an Agilent 1260 Infinity II Prime LC (Germany).

2.4. Estimation of photocatalytic performance

The photocatalytic performance of as prepared catalysts was estimated by photoreduction of U(VI) and selective preparation of BD at 25 ℃. Generally, 20 mg as prepared material was mixed with 50 mL of a solution consisting with 20 mg/L of U(VI) and 0.1 mol/L BA. After that, HNO_3 (0.1 M) and NaOH (0.1 M) solutions were employed to regulate the suspension's pH value. Before illumination, the mixture was put in the dark for 30 min to obtain adsorption-desorption equilibrium. Then, the suspension was illuminated by a Xe lamp (300 W) light source equipped with a 420 nm cut-off filter. Every certain time, a tiny portion of suspension was taken out and filtered by a 0.22 μm syringe membrane, and the uranyl concentration was measured via Arsenazo-III spectrophotometry [31], while the concentrations of the remaining BA and resulting BD after oxidation were quantitatively conducted via HPLC. For comparison, similar control experiments (including no

addition of photocatalyst) were operated. Likewise, the effect of coexisting ions experiments was only performed with the additional addition of other ions (M(Cl)$_n$, (M = metal ions) and K$_n$X, (X = anions)) under the same conditions. Finally, the photoreduction percent of U(VI) was figured out according to the previously reported means [31], and the conversion percentage of BA and the selectivity for BD were determined with the formulas below:

$$Conversion(\%) = [(C_S - C_{BA})/C_S] \times 100\% \qquad (1)$$

$$Selectivity(\%) = [C_{BD} - (C_S - C_{BA})] \times 100\% \qquad (2)$$

Here, C_S represented the starting BA concentration, whereas C_{BA} and C_{BD} represented the concentrations of the residual BA and produced BD after the photo-oxidation reaction, respectively.

2.5. Computation details

First-principles calculations of the electronic work function and active oxygen adsorption energy of WO$_x$/g-C$_3$N$_4$ heterojunction semiconductors with calculation model shown in Fig. S1 (Supplementary Material) were estimated by employing the Vienna ab initio Simulation Package (VASP 5.4.4) code [32,33]. The electron exchange correlation potential was described using the Perdew-Burke-Ernzerhof (PBE) [34] exchange-correlation functional in a generalized gradient approximation (GGA) [35], while the ion−electron interaction was described using a projector augmented wave (PAW) pseudo-potentials [36] with a cutoff energy of 500 eV. The DFT-D$_3$ method with Becke–Johnson damping [37,38] was adopted to describe the apparent van der Waals (vdW) interaction between g-C$_3$N$_4$ and WO$_x$, with the minimum distance of 2.73 Å in WO$_x$/g-C$_3$N$_4$ heterojunction. A vacuum layer with a thickness exceeding 18 Å was used in the Z-direction to prevent the influence of periodic structures. When the maximal residual energy and the force in the optimization process were less than 1×10^{-5} eV and 0.05 eV/Å, respectively, the system reached the convergence standard. Geometric optimization and work function calculations were used Monkhorst-Pack k-point mesh. For geometric optimization of the crystal structures of isolated WO$_3$ and g-C$_3$N$_4$, $5 \times 5 \times 4$ and $9 \times 9 \times 8$ k-point mesh was used, respectively. The optimal lattice constants were $7.40 \times 7.57 \times 7.72$ and $7.13 \times 7.13 \times 6.68$, respectively, which were consistent with the experimental data in the reference [39,40]. The optimized crystals with 001 plane for g-C$_3$N$_4$ and 002 plane for WO$_3$ were combined by using Vaspkit software [41] to construct a WO$_3$/g-C$_3$N$_4$ heterojunction with a crystal mismatch rate less than 5% which was composed of 48 C atoms, 64 N atoms, 144 O atoms and 48 W atoms and the lattice constants were a= 27.4 Å, b= 14.6 Å, γ = 58.1°. The heterojunction structure of WO$_3$/g-C$_3$N$_4$ was optimized and further used for calculating the oxygen adsorption energy and the optimal structure of WO$_x$/g-C$_3$N$_4$. There were three types of oxygen in WO$_3$/g-C$_3$N$_4$. Therefore, when optimizing WO$_x$/g-C$_3$N$_4$, these three different types of oxygen were removed from WO$_3$/g-C$_3$N$_4$ (shown in Fig. S2) separately, and the configuration with the lowest energy was considered the most likely location for oxygen atoms to be defective. The optimal structure was used for electronic work function and oxygen species adsorption calculation. For geometric optimization, electronic work function of WO$_3$/g-C$_3$N$_4$ and WO$_x$/g-C$_3$N$_4$ heterojunction, $2 \times 2 \times 1$ and $4 \times 4 \times 1$ k-point mesh was used, respectively.

3. Results and discussion

3.1. Characterization of the photocatalysts

Through XRD and FT-IR measurements, we first examined the crystallographic properties and functional group information. Fig. 1a depicts the XRD patterns of the prepared materials. In the XRD patterns of WO$_x$ and WO$_x$/g-C$_3$N$_4$, the characteristic diffraction peaks located at 22.9° and 23.6° correlated to the (002) and (200) planes of the monoclinic phase WO$_3$, respectively, which was in agreement with the proceeding study [42]. Whereas the peaks corresponding to these same crystal plane in WO$_3$ were 23.1° and 24.4°, respectively. Comparing the XRD of WO$_3$ and WO$_x$, WO$_3$/g-C$_3$N$_4$ and WO$_x$/g-C$_3$N$_4$, respectively, it was discovered that the presence of oxygen vacancies raised the lattice constant and shifted the distinctive diffraction peaks of WO$_x$ toward narrower diffraction angles [23]. Overall, for all obtained samples, the diffraction patterns of WO$_x$ and WO$_3$ matched well against the reference monoclinic phase WO$_3$ (JCPDS 83–0951). Furthermore, the g-C$_3$N$_4$ diffraction pattern displayed two primary peaks located at roughly 13.0° and 27.5°, which corresponded to the tri-s-triazine rings system stacking (100) facet and the interlayer stacking (002) facet in g-C$_3$N$_4$, respectively [43]. All of the typical diffraction peaks of WO$_x$ and g-C$_3$N$_4$ emerged in the WO$_x$/g-C$_3$N$_4$ composite. Meanwhile, due to the low WO$_x$ content in the WO$_x$/g-C$_3$N$_4$ sample, the characteristic diffraction peaks of WO$_x$ were very weak in XRD of WO$_x$/g-C$_3$N$_4$.

According to Fig. 1b, the FT-IR spectra of WO$_3$/g-C$_3$N$_4$ and WO$_x$/g-C$_3$N$_4$ equally featured all the distinctive peaks that g-C$_3$N$_4$ has. The peak
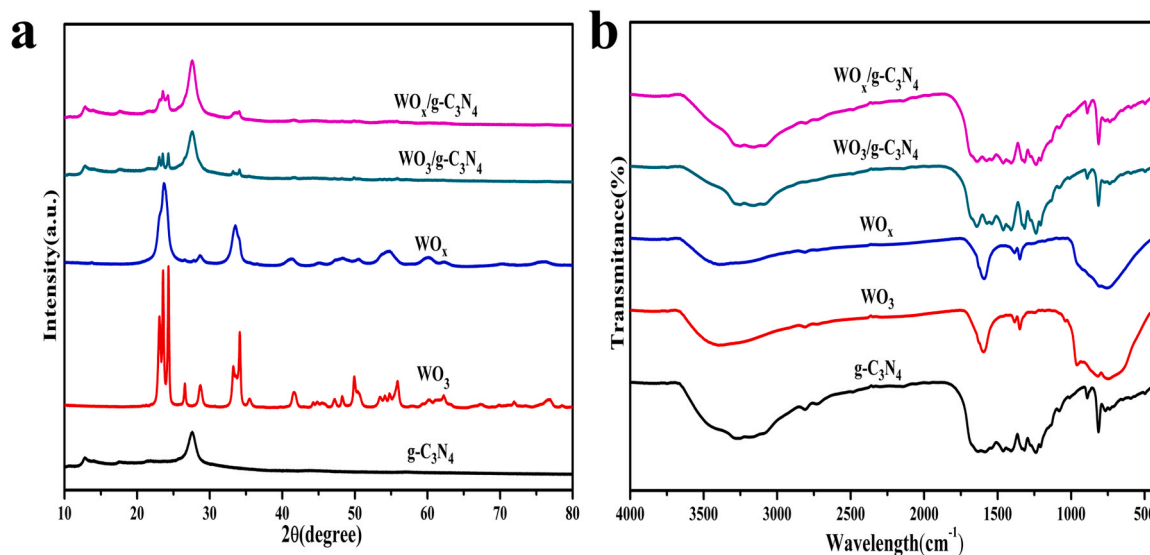

Fig. 1. XRD patterns of g-C$_3$N$_4$, WO$_3$, WO$_x$, WO$_3$/g-C$_3$N$_4$ and WO$_x$/g-C$_3$N$_4$ composites (a); FT-IR spectra of g-C$_3$N$_4$, WO$_3$, WO$_x$, WO$_3$/g-C$_3$N$_4$ and WO$_x$/g-C$_3$N$_4$ composites (b).

situated around 3274 cm^{-1} may relate with the stretching vibrations of -NH/-NH$_2$ groups [44]. Peaks in the range of 1170–1700 cm^{-1} were assigned to the CN heterocyclic compound in stretching vibration modes [45]. In addition, the characteristic peak observed around 809 cm^{-1} corresponded to the classic tri-s-triazine ring [46]. In terms of WO$_x$ and WO$_3$, the absorption bands appearing at 450–1000 cm^{-1} were induced by the W-O-W and O-W-O stretching modes [47]. Whereas the peaks occurred at 3396 cm^{-1} and 1595 cm^{-1} came from the O-H stretching vibration and bending vibration of the H$_2$O adsorbed on WO$_3$ and WO$_x$, respectively. Furthermore, FT-IR spectra showed comparable results to XRD. Due to the low amount of WO$_x$ in the WO$_x$/g-C$_3$N$_4$ composites, the distinctive peaks of WO$_x$ were feeble in oxygen deficient WO$_x$/g-C$_3$N$_4$ FT-IR spectrum.

SEM was used to characterize the surface microstructure of the samples. As shown by Fig. 2a, bare g-C$_3$N$_4$ exhibits irregularly stacked lamellar structures. WO$_x$ sample had a flaky morphology (Fig. 2b). And SEM images of the WO$_x$/g-C$_3$N$_4$ composite (Figs. 2c-2d) showed that the WO$_x$ flakes were homogeneously deposited on g-C$_3$N$_4$, making the composites rougher than bare g-C$_3$N$_4$, increasing the specific surface area, and providing more reactive sites for photocatalysis. Moreover, the elemental mapping images (Figs. 2e-2f) verified the coexistence of C, N, O, and W elements.

To further explicate the elemental composition of the as-prepared samples, XPS spectra were studied. Fig. 3a showed that C, N, O, and W elements coexist in WO$_x$/g-C$_3$N$_4$ composite. As shown by the O1s XPS spectra (Fig. 3b), the peak of 530.5 eV arose from the lattice oxygen of WO$_3$ [29], but it drifted to lower energy 530.1 eV in WO$_x$/g-C$_3$N$_4$. In particular, WO$_x$/g-C$_3$N$_4$ had an additional wide peak (532.6 eV), and this belonged to the adsorbed oxygen species at oxygen vacancies [42]. In other words, the XPS of O1s indicated that there were oxygen vacancies on the surface of WO$_x$/g-C$_3$N$_4$. Moreover, similar variations were seen in the W4f spectra (Fig. 3c), where W4f$_{7/2}$ and W4f$_{5/2}$ for

WO$_x$/g-C$_3$N$_4$ possessed binding energies of 35.1 and 37.2 eV, respectively, which were lower than those of pure WO$_3$ (35.5 and 37.6 eV). Fig. 3d exhibited C1s spectra, where the two peaks of g-C$_3$N$_4$ and WO$_x$/g-C$_3$N$_4$ at 288.3 and 288.5 eV, respectively, may be related to the N—C≡N bond in g-C$_3$N$_4$ [48]. As shown by N1s spectra (Fig. 3e), the N1s spectrum of WO$_x$/g-C$_3$N$_4$ could be disaggregated as three independent peaks (399, 400.4, and 401.5 eV), corresponding to C≡N-C, N-(C)$_3$ and -NH$_2$, respectively [44], and were more positive than those of bare g-C$_3$N$_4$ (398.8, 400.2, and 401.3 eV). According to all the XPS spectra, after close contact, the charges appeared to migrate from g-C$_3$N$_4$ to WO$_x$ across their interface. Additionally, room temperature ESR analyses were performed to verify the reality of oxygen vacancies. Around the center of g = 2.003, the typical ESR symmetric signals of WO$_x$ and WO$_x$/g-C$_3$N$_4$ could be observed in Fig. 3f, which were attributed to single electron trapping at oxygen vacancies [49]. In contrast, the signal of WO$_3$ was extremely feeble. All these suggested that WO$_x$ and WO$_x$/g-C$_3$N$_4$ contained a significant amount of oxygen vacancies. The oxygen defect might be caused by the treatment of Na$_2$WO$_4$·2 H$_2$O with glucose as the reducing agent during the preparation of its precursor material (WO$_3$·H$_2$O). Due to the reducing property of glucose, the prepared WO$_3$·H$_2$O contained a large number of oxygen vacancies. This oxygen vacancy-rich WO$_3$·H$_2$O was calcined at high temperature under nitrogen protection, losing only the water of crystallization and leaving behind abundant oxygen vacancies, which ultimately formed an oxygen-deficient WO$_x$. On the contrary, when it was calcined at high temperature in air, the missing lattice oxygen in WO$_3$ was filled in by the oxygen in the air, resulting in the formation of defect-free WO$_3$ [42]. Given the above, it is evident that oxygen deficient WO$_x$/g-C$_3$N$_4$ composite was synthesized effectively.

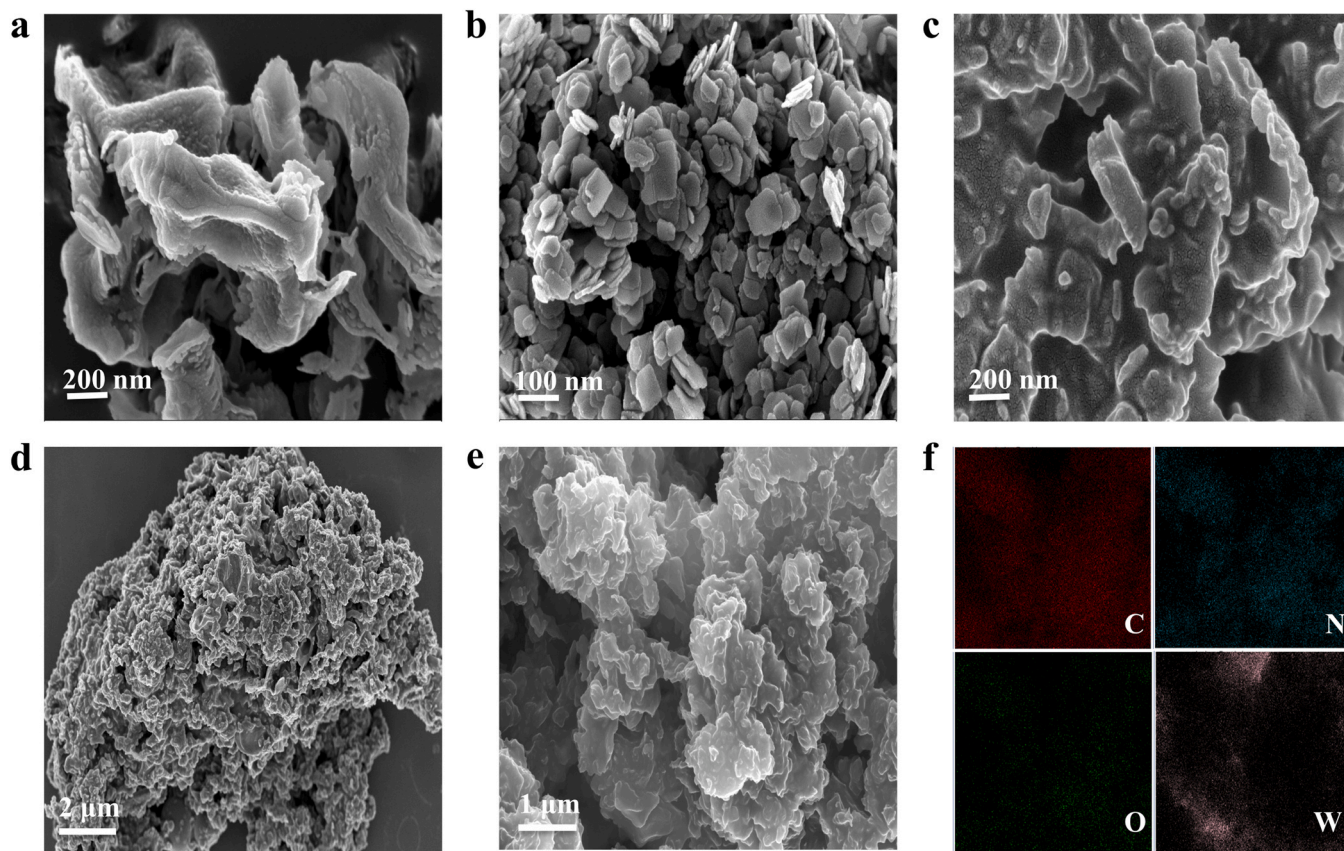**Fig. 2.** SEM images of g-C$_3$N$_4$ (a), WO$_x$ (b) and WO$_x$/g-C$_3$N$_4$ (c-d); Elemental mapping images of WO$_x$/g-C$_3$N$_4$ (e-f).

Fig. 3. The XPS spectra of $WO_x/g-C_3N_4$ (a); High resolution O 1 s XPS spectra of WO_3 and $WO_x/g-C_3N_4$ (b); High resolution W 4 f XPS spectra of WO_3 and $WO_x/g-C_3N_4$ (c); High resolution C 1 s XPS spectra of $g-C_3N_4$ and $WO_x/g-C_3N_4$ (d); High resolution N 1 s XPS spectra of $g-C_3N_4$ and $WO_x/g-C_3N_4$ (e); Room temperature ESR spectra of WO_3, $WO_x/g-C_3N_4$ and WO_x (f).

3.2. Optical and electrical properties

Semiconductor's energy band structure is a determinant factor affecting photocatalytic performance. The UV–vis–DRS of all the prepared photocatalysts are displayed by Fig. 4a. Compared with bare $g-C_3N_4$, the absorption margin of $WO_x/g-C_3N_4$ was clearly red-shifted with a significant increment in absorbance intensity, which would doubtless enhance visible light utilization. According to Tauc curves and Kubelka-Munk equation, the band gaps (E_g) of $g-C_3N_4$, WO_3 and WO_x were inferred as 2.77 eV, 2.64 eV and 2.18 eV respectively (Fig. 4b). In addition, the XPS valance band (VB) spectra (Fig. 4c) manifested that the band gaps between Fermi level (E_f) and VB for $g-C_3N_4$, WO_3 and WO_x were 1.49 eV, 2.12 eV and 1.76 eV, respectively. Whereas the Mott-Schottky curves (Figs. 4d-4f) revealed that the flat-band potentials (generally considered as E_f) [50] of $g-C_3N_4$, WO_3 and WO_x relative to Ag/AgCl were − 0.57 V, − 0.61 V and − 0.51 V, respectively. Besides, their corresponding reversible hydrogen electrode (RHE) potentials were converted with the equation below [51]:

$$E_{(RHE)} = E_{(Ag/AgCl)} + 0.198eV + 0.0592pH \qquad (3)$$

Here, the pH of the 0.1 M Na_2SO_4 electrolyte solution was 6.1, and thus the converted E_f for $g-C_3N_4$, WO_3 and WO_x were determined with the values of − 0.01 eV, − 0.05 eV and 0.05 eV, respectively. Combined with all the above experimental results, the VB potentials were + 1.48 eV, + 2.07 eV and + 1.81 eV for $g-C_3N_4$, WO_3 and WO_x, respectively. Consequently, the CB potentials could be deduced as − 1.29 eV, − 0.57 eV and − 0.37 eV, corresponding to $g-C_3N_4$, WO_3 and WO_x. Accordingly, the energy band structure diagrams were constructed

in Fig. 4g. Considering the energy band structures of $g-C_3N_4$ and WO_x, there are two possible heterogeneous structure formation modes, including type II and Z-scheme. And the locations where the oxidation and reduction reactions are completely different for these two heterojunction modes. If $WO_x/g-C_3N_4$ is a type II heterojunction, U(VI) reduction reaction should occur on WO_x and oxidation will take place on $g-C_3N_4$. On the contrary, if $WO_x/g C_3N_4$ is a Z-scheme heterojunction, $g-C_3N_4$ will become the reducing end and WO_x will become the oxidizing end. In order to figure out which type of $WO_x/g-C_3N_4$ heterojunction, mapping images of elemental distribution for $WO_x/g-C_3N_4$ composites after U(VI) photo-deposition were investigated. The outcomes, illustrated in Fig. 4h, the mapping image of the distribution of U was consistent with that of C and N, but differed from that of W. It implied that U(VI) photoreduction took place on $g-C_3N_4$, and the corresponding oxidation reaction was carried out on WO_x, indicating a Z-scheme heterojunction of $WO_x/g-C_3N_4$.

Additionally, the system's work function was investigated to determine the charge transfer and separation that occurred after WO_x and $g-C_3N_4$ formed a heterojunction by DFT simulations. As shown in Figs. (5a-5c), when a stable $WO_x/g-C_3N_4$ heterojunction was established, the electron work function for $WO_x/g-C_3N_4$ heterojunction (5.99 eV) lied between WO_x (6.24 eV) and $g-C_3N_4$ (4.63 eV) and $g-C_3N_4$'s was smaller than WO_x's. Therefore, electrons would migrate to WO_x from $g-C_3N_4$ before their Fermi levels were in equilibrium. And the WO_x would gain e^- and become negatively charged, whereas the $g-C_3N_4$ would lose e^- and become positively charged. As the positive and negative charges were separated, an internal electronic field would be induced from $g-C_3N_4$ to WO_x. Consequently, the band edges of $g-C_3N_4$ and WO_x would be bent towards up and down, respectively, due to the internal electronic field.
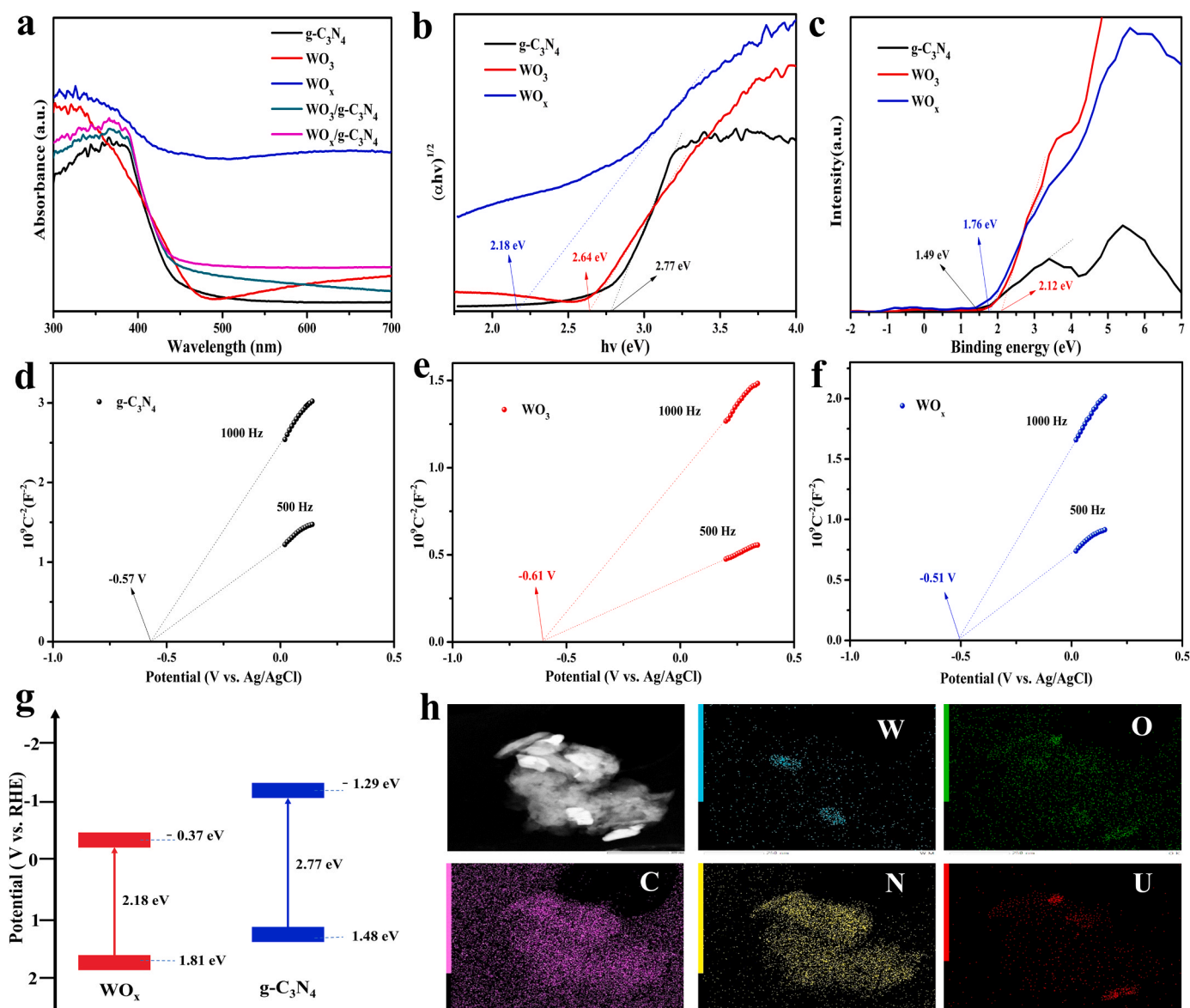
Fig. 4. UV–vis diffuse reflectance spectra (a); Tauc plots for g-C_3N_4, WO_3 and WO_x (b); XPS valance band spectra of g-C_3N_4, WO_3 and WO_x (c); The Mott-Schottky curves of g-C_3N_4 (d), WO_3 (e) and WO_x (f); Illustration of the energy band structure of WO_x and g-C_3N_4 (g); Elemental distribution mapping images of WO_x/g-C_3N_4 after U(VI) photo-deposition (h).

Ultimately, the aforementioned internal electronic field would lead to the reorganization between photoexcited e$^-$ coming from the CB of WO_x and photoexcited h$^+$ coming from the VB of g-C_3N_4, resulting in a Z-type heterojunction [52]. At the same time, e$^-$ from the CB of g-C_3N_4 and h$^+$ from the VB of WO_x were accumulated, triggering specific reduction and oxidation reactions. In a word, this Z-type heterojunction can well retain the photoinduced e$^-$ in g-C_3N_4's CB and the photogenerated h$^+$ in WO_x's VB, resulting in photoreduction on the g-C_3N_4 surface and oxidation reaction on WO_x surface. This calculation was in accordance with the outcomes of photo-deposition of uranyl (Fig. 4h).

To evaluate the separation and transmission of the photoexcited e$^-$-h$^+$ pairs, PL emission spectra, electrochemical impedance spectroscopy (EIS) and transient current responses spectra have been investigated. As can be seen from Fig. 5d, the fluorescence emission intensity followed the following order: g-C_3N_4 > WO_3/g-C_3N_4 > WO_x/g-C_3N_4 > WO_x > WO_3, where g-C_3N_4 and WO_3/g-C_3N_4 were stronger, WO_x/g-C_3N_4 was weaker, WO_x and WO_3 was very weak, and the fluorescence intensity of WO_x/g-C_3N_4 is slightly stronger than that of WO_x. It might be the establishment of a heterojunction between WO_x and g-C_3N_4, which

produced a significant amount of photoinduced e$^-$ in the presence of light, as supported by the photocurrent intensity (Fig. 5f). And the growth rate of its photoinduced e$^-$ might be faster than the migration rate, leading the slightly stronger fluorescence intensity of WO_x/g-C_3N_4 than WO_x. Whereas the emission intensity of WO_x was slightly higher than that of WO_3 was due to the excitonic PL spectrum, which reflected the higher concentration of oxygen vacancies on the surface of WO_x [53]. Moreover, the experiments of electrochemical impedance spectra (Fig. 5e) showed that the semicircle was WO_x/g-C_3N_4 < WO_3/g-C_3N_4 < WO_x < WO_3 < g-C_3N_4. In other words, the results of the above two experiments indicated that both forming of WO_x/g-C_3N_4 heterojunction and oxygen vacancies on WO_x contributed to the charges separation and transmission at the contact interface. Besides, the transient current responses of all the samples were compared in Fig. 5f. Apparently, WO_x/g-C_3N_4 featured the strongest transient response, whereas g-C_3N_4 featured the weakest, which corresponded exactly to the results of EIS (Fig. 5e). In summary, optical and electrical property characterizations verified that the WO_x/g-C_3N_4 composite would be excellent at utilizing visible light and photogenerated charges, leading to superb
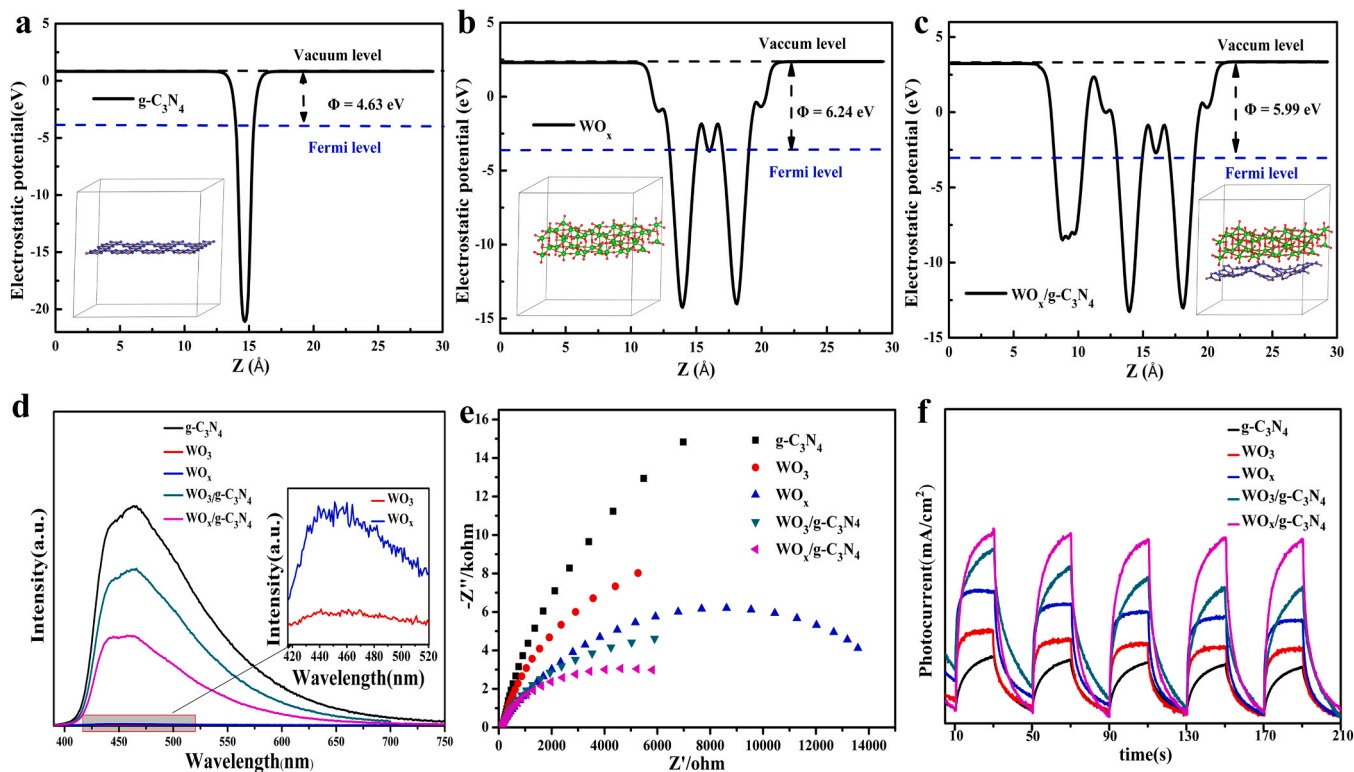
Fig. 5. Electrostatic potential with the Z-direction of g-C$_3$N$_4$ (a), WO$_x$ (b) and WO$_x$/g-C$_3$N$_4$ (c) heterojunction. Insets illustrated optimal material configuration for electronic work function calculation; PL emission peaks (d); Electrochemical impedance spectra (e); Transient photocurrent response spectra (f).

photocatalytic activity.

3.3. Photocatalytic activity

Batch experiments were conducted to study the performance of the synthesized catalysts for photoreduction of U(VI) and preparation of BD under simulated sunlight irradiation. As illustrated by Fig. 6a, no change in U(VI) concentration was observed in the absence of catalyst, suggesting ignorable self-catalysis. But, in the presence of the synthesized catalysts, the elimination of U(VI) occurred. And the removal efficiencies of U(VI) by WO$_x$ and WO$_x$/g-C$_3$N$_4$ were remarkably higher than that by WO$_3$ and WO$_3$/g-C$_3$N$_4$, respectively. Among these catalysts, g-C$_3$N$_4$ exhibited the worst removal rate, while WO$_x$/g-C$_3$N$_4$ was the best. Furthermore, WO$_x$/g-C$_3$N$_4$ achieved a maximum of 98.5% removal ratio of U(VI) after 120 min irradiation. Moreover, the photoreduction rate constants (k) of the prepared catalysts were calculated (Fig. S3). The k values were 0.00317, 0.00475, 0.00368, 0.01126 and 0.03306 min^{-1}, corresponding to g-C$_3$N$_4$, WO$_3$, WO$_x$, WO$_3$/g-C$_3$N$_4$ and WO$_x$/g-C$_3$N$_4$, respectively.

In addition, the role of oxygen in the reaction system was further investigated by photocatalytic reaction activity experiments under different atmospheres (air, pure O$_2$ and pure N$_2$) with WO$_x$/g-C$_3$N$_4$ as catalyst (Fig. 6b). To ensure the reaction was carried out under the corresponding atmosphere, pure N$_2$ and O$_2$ were drummed into the reaction system for 1 h before the reaction (except for the experiment in air atmosphere), respectively. Intriguingly, the removal ratio of U(VI) under pure O$_2$ atmosphere was higher than that under pure N$_2$ environment, but lower than that under air conditions, indicating that O$_2$ acted as a double-edged sword in the photoreduction reaction.

Meanwhile, the impact of different catalysts for selective oxidation of BA to BD was investigated. As shown in Fig. 6c and Fig. S4, the single g-C$_3$N$_4$, bare WO$_3$, WO$_x$, WO$_3$/g-C$_3$N$_4$ and WO$_x$/g-C$_3$N$_4$ as catalysts showed 2.6%, 9.2%, 14.6%, 19.1% and 32.1% BA conversions after 2 h of light exposure, respectively. While the selectivity of WO$_3$/g-C$_3$N$_4$ and

WO$_x$/g-C$_3$N$_4$ for BD was 76.4% and 98.1%, respectively. Although WO$_3$/g-C$_3$N$_4$ resulted in higher BA conversion than single g-C$_3$N$_4$ and WO$_3$, and even higher than WO$_x$. Regrettably, benzoic acid was identified in the oxidation products catalyzed by WO$_3$/g-C$_3$N$_4$, indicating that BD underwent further oxidation, resulting in a decrease in oxidation selectivity. Gladly, the conversion of BA by WO$_x$/g-C$_3$N$_4$ was approximately 32.1%, and it was not only better than those by single g-C$_3$N$_4$, WO$_3$, WO$_x$, and the composite WO$_3$/g-C$_3$N$_4$, but no benzoic acid was found in the final oxidation products. Amazingly, its selectivity was close to 98.1%, preferable to that of WO$_3$/g-C$_3$N$_4$. These results illustrated that the presence of oxygen vacancies and forming of WO$_x$/g-C$_3$N$_4$ heterojunction enhanced the removal rate of uranyl as well as the selective oxidation of BA to BD. Furthermore, as with U(VI) reduction studies, the effect of different atmospheric conditions on the conversion of BA to BD was also investigated. On the contrary, the conversion of BA had a sequence as follow: O$_2$ > Air > N$_2$ (Fig. 6d and Fig. S5) in diverse atmospheres, which implied that oxygen acted as an essential role during the oxidation process of BA. Overall, an appropriate amount of oxygen facilitated WO$_x$/g-C$_3$N$_4$ photocatalytic reduction of uranyl and selective oxidation from BA to BD, and this photocatalytic system showed satisfactory results at both the oxidation and reduction ends in the air environment.

And the reasons for the above may be mainly ascribed to the following aspects. Firstly, the oxygen vacancies shrink the bandwidth, extend the range of absorbable light and raise photon utilization. Secondly, the presence of oxygen vacancies and forming of WO$_x$/g-C$_3$N$_4$ heterojunction accelerate the disjunction of e$^-$ and h$^+$, as evidenced by the PL emission spectra (Fig. 5d) and transient photocurrent response (Fig. 5f). Thirdly, the oxygen vacancies are favorable for oxygen trapping, strengthening the •O$_2^-$ generation capability, as confirmed by the ESR spectra of •O$_2^-$ trapping (Fig. 6e) and XPS of WO$_x$/g-C$_3$N$_4$ (Fig. 3b). Owing to the fact that WO$_x$/g-C$_3$N$_4$ owns a stronger ability in generating •O$_2^-$ than WO$_3$/g-C$_3$N$_4$, accelerating the conversion of BA, and thus enhancing the performance of both ends of the photocatalytic system
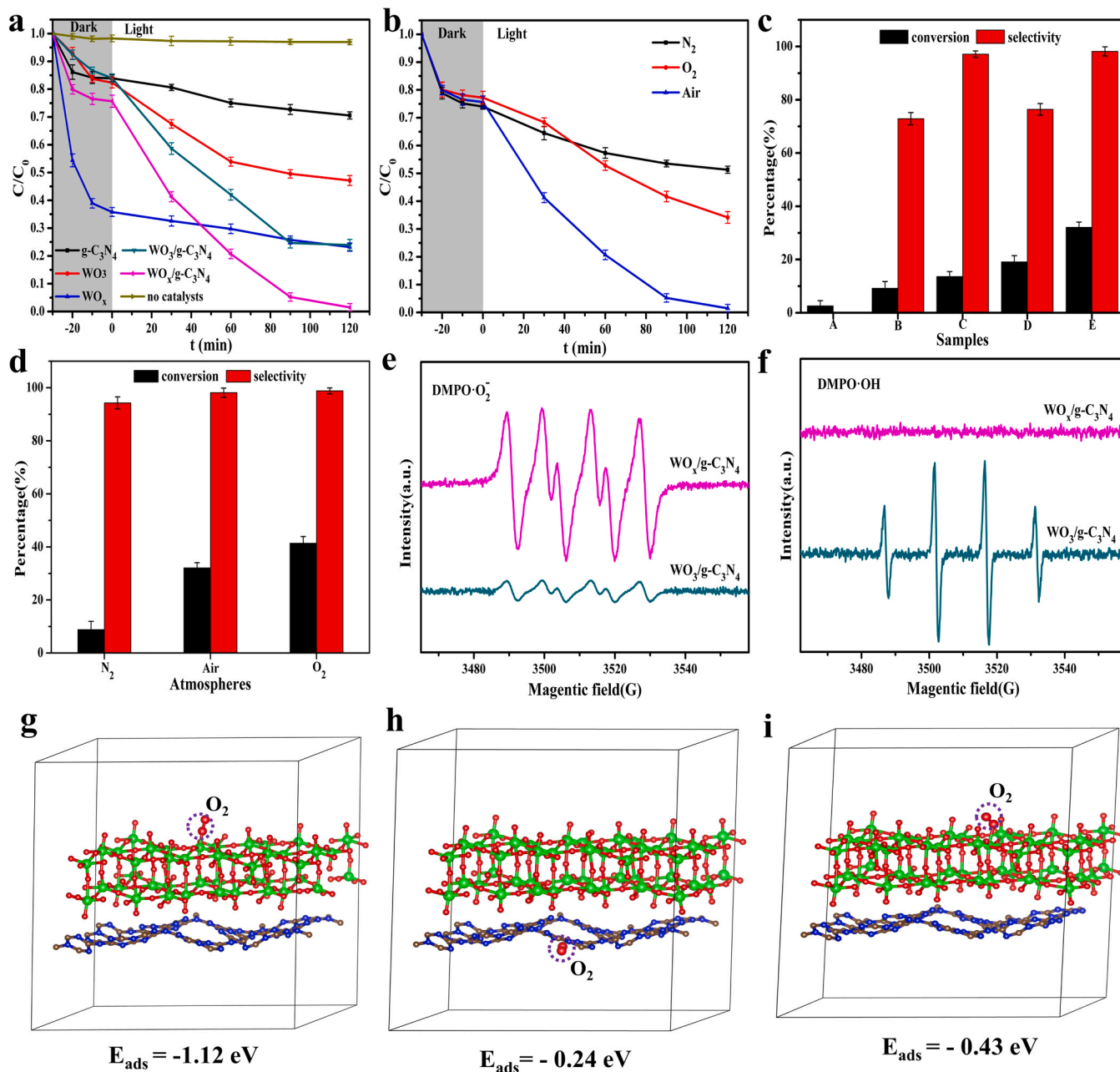
Fig. 6. Photoreduction performance of U(VI) with different catalysts, (pH = 3.8, air) (a); The influence of different atmospheres on the removal ratio of U(VI) with $WO_x/g\text{-}C_3N_4$ as catalyst (b); Selective oxidation performance of BA with different catalysts (A) $g\text{-}C_3N_4$, (B) WO_3, (C) WO_x, (D) $WO_3/g\text{-}C_3N_4$ and (E) $WO_x/g\text{-}C_3N_4$ (c); Effect of different atmospheres on the selective oxidation of BA with $WO_x/g\text{-}C_3N_4$ as catalyst (d). ESR spectra of $\bullet O_2^-$ radical (illumination for 10 min) (e); ESR spectra of $\bullet OH$ radical (illumination for 10 min) (f); The optimal geometric structure and adsorption energy of O_2 adsorption on different surfaces. Oxygen on WO_x surface (g) and $g\text{-}C_3N_4$ (h) in $WO_x/g\text{-}C_3N_4$ heterojunction and WO_3 surface (i) in defect-free $WO_3/g\text{-}C_3N_4$ heterojunction.

simultaneously. To further elucidate the effect of introducing oxygen vacancies on oxygen adsorption and activation, we calculated the adsorption energy of O_2 on the defect-free $WO_3/g\text{-}C_3N_4$ surface and the $WO_x/g\text{-}C_3N_4$ surface with oxygen defects using DFT calculations. The adsorption energy equation was shown in Eq. 4.

$$E_{ads} = E_{WO_x/g-C_3N_4+O_2} - E_{WO_x/g-C_3N_4} - E_{O_2} \qquad (4)$$

Where E_{ads}, $E_{WO_x/g-C_3N_4+O_2}$ and $E_{WO_x/g-C_3N_4}$ denoted the energy difference before and after oxygen adsorption by $WO_x/g\text{-}C_3N_4$ and its total energy with and without adsorbed O_2 molecules, respectively. The same equation was used for the adsorption on the defect-free system. A

negative binding energy implied that the adsorption procedure was energetically advantageous. As seen from Figs. 6g-6i, for $WO_x/g\text{-}C_3N_4$ heterojunction, the adsorption energy of O_2 on WO_x's surface (−1.12 eV) was significantly more negative than that of $g\text{-}C_3N_4$ (−0.24 eV), suggesting that O_2 was most readily adsorbed on the surface of WO_x in $WO_x/g\text{-}C_3N_4$ heterojunction. And comparing $WO_x/g\text{-}C_3N_4$ and $WO_3/g\text{-}C_3N_4$ heterojunctions, the adsorption energy of O_2 on WO_x's surface was significantly more negative than that on WO_3's surface (−0.43 eV), indicating that the oxygen defects favor O_2 adsorption, leading to a significant difference $\bullet O_2^-$ radical generation capacity. This was also consistent with the outcomes of preceding ESR experiments (Fig. 6e). Interestingly, for $WO_x/g\text{-}C_3N_4$, WO_x's surface mainly accumulated photoinduced h^+, while $g\text{-}C_3N_4$'s surface accumulated

photogenerated e⁻. Based on the above discussions, obviously, the introduction of oxygen vacancies caused O_2 to be immobilized at the oxidation end of the system (WO_x). Fourthly, since the oxidation of BA caused by vacancies requires the participation of oxygen [54], an appropriate amount of oxygen would encourage BA to consume holes, thereby improving the disjunction of e⁻-h⁺ pairs and ultimately resulting in an increase in catalytic efficiency. While oxygen was in excess, on the other hand, only a portion of oxygen would be consumed by BA at the oxidation end, and the excess O_2 would battle with U(VI) for electrons at the reduction side. And from the above, it was clear that g-C_3N_4's CB potential (−1.28 eV, reduction end of WO_x/g-C_3N_4) was more negative than that of O_2/•O_2^- (−0.33 eV), revealing that photoinduced e⁻ reduced U(VI) more readily than •O_2^-, i.e., the reduction rate of U(VI) would be decreased if O_2 first competed with U(VI) for e⁻ at reduction side and then reduced U(VI). And the bubbling of N_2 into the reaction solution would drive away the dissolved O_2, thereby reducing the oxidation of BA involved by oxygen and holes, i.e., the holes consumption decreased, leading to a decrease in photocatalytic performance.

As reported in the literatures [55,56], in the photocatalytic selective oxidation of BA, if •OH were generated during the catalytic oxidation, it would further oxidize BD and reduce the selectivity. And from the above, it was clear that the VB potentials of WO_x (+1.81 eV) and g-C_3N_4 (+1.48 eV) were less positive than OH⁻/•OH (+1.99 eV vs. NHE) [57], such that it was difficult to produce strong oxidizing •OH radical (Fig. 6f). When WO_x/g-C_3N_4 was used as the catalyst, the selectivity was good. But WO_3's VB potential (+2.07 eV) was more positive than OH⁻/•OH, leading to •OH generation, which was confirmed by Fig. 6f, and there would be excessive oxidation when WO_3/g-C_3N_4 was used as a catalyst, thus reducing the selectivity.

As we all know, the uranyl species and the surface potential of

catalyst depend on the pH of aqueous solution [58], both of which are critical determinants affecting the photoreduction of U(VI). Thus, the photocatalytic performance of WO_x/g-C_3N_4 for U(VI) was examined at various pH levels (Fig. 7a). As the pH of the solution increased from 2.8 to 3.8, an increase of U(VI) removal from near zero to a maximum value 98.5%, while it gradually decreased as the pH increased further from 3.8 to 6.8. All is related to the surface potential of the catalyst and the U(VI) species. As shown by Fig. 7b, the surface potential of WO_x/g-C_3N_4 was positive at pH 2.8–3.3, became negative at pH 3.8–4.8, and finally became positive again at pH 5.3–6.8. Moreover, the U(VI) species were predominantly UO_2^{2+} in the pH range of 2.8–4.8, and UO_2^{2+}, $(UO_2)_2(OH)_2^{2+}$ and $(UO_2)_3(OH)_5^+$ in the pH range of 5.3–6.8 according to preceding work [59], meaning that the uranium species state in that pH range was positively charged. From the above, it was clear that both the charge of U(VI) species and the surface potential of WO_x/g-C_3N_4 are positive at the pH range from 2.8 to 3.3 and from 5.3–6.8, resulting mutual electrostatic repulsion between the U(VI) and catalyst, then impeding the elimination of U(VI). However, since they featured opposite charges at pH 3.8, 4.3 and 4.8, they were electrostatically attracted to each other. Notably, the zeta potential of WO_x/g-C_3N_4 had the most negative value at pH = 3.8, leading to the best photoreduction performance.

Furthermore, the reusability of WO_x/g-C_3N_4 was tested using cycling experiments. After each photocatalytic reaction, the material was gathered by centrifugation and washed three times sequentially with 0.1 M Na_2CO_3 and deionized water, dried, and then reused. From Fig. 7c, the U(VI) removal ratio decreased by only about 10% after five rounds of recycling, demonstrating the stability in long-term use.

To facilitate practical applications, interfering ions were investigated for their effect on the elimination of U(VI) by WO_x/g-C_3N_4.
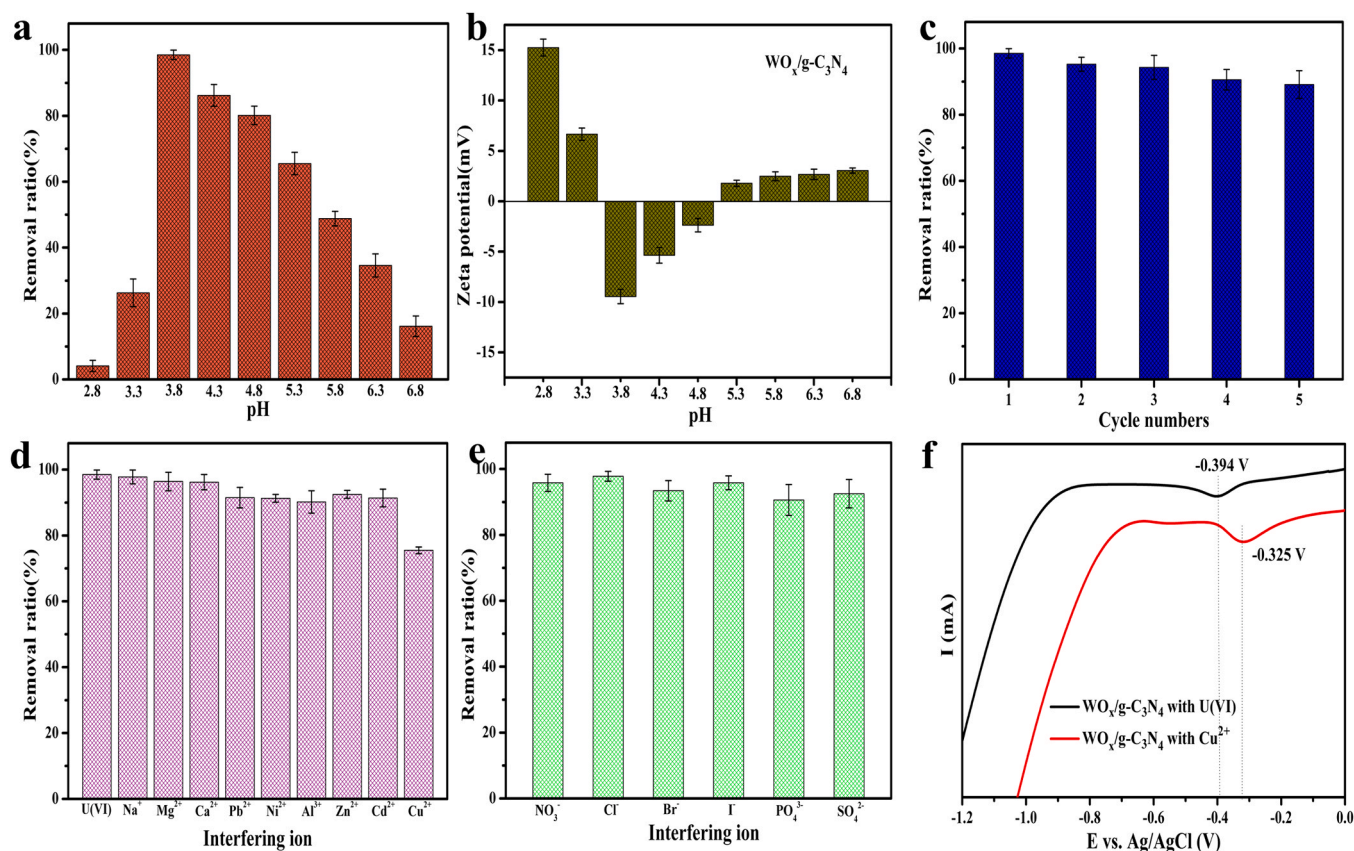

Fig. 7. The U(VI) removal ratio by WO_x/g-C_3N_4 at different pH value (a); The zeta potential of WO_x/g-C_3N_4 at different pH (b); The U(VI) photoreduction performance during five cycling runs (c); The impacts of the metal cations ([M] = 40 mg/L, M= metal ions) on U(VI) removal (d) and the influences of the non-metal anions ([X]= 40 mg/L, X = non-metal anions) on U(VI) removal (e), pH = 3.8; Linear sweep voltammetry curves of WO_x/g-C_3N_4 with different metal ions, [U(VI)] = 20 mg/L, [Cu^{2+}] = 40 mg/L, C_{NaNO3} = 0.5 M, pH = 3.8 (f).

Consequently, 40 mg/L of various metal ions or non-metal anions was introduced into the system employing $WO_x/g\text{-}C_3N_4$ as the catalyst to run the photocatalytic reaction, respectively, and their corresponding removal ratios were acquired (Figs. 7d and 7e). As shown in Figs. 7d and 7e, when interfering cations (Na^+, Mg^{2+}, Ca^{2+}, Pb^{2+}, Ni^{2+}, Al^{3+}, Zn^{2+}, Cd^{2+} and Cu^{2+}) were present, the removal rates of U(VI) by $WO_x/g\text{-}C_3N_4$ were 97.8%, 96.4%, 96.2%, 91.5%, 91.3%, 90.2%, 92.5%, 91.4% and 75.5%, respectively. It was clear that the removal efficiency of uranyl exceeded 90% in all cases except for Cu^{2+}. Furthermore, the removal rates of uranyl also exceeded 90.6% in the presence of all tested anions (NO_3^-, Cl^-, Br^-, I^-, PO_4^{3-} and SO_4^{2-}), indicating the excellent anti-interference capability of $WO_x/g\text{-}C_3N_4$. To clarify the reason for the presence of Cu^{2+} interference, the linear sweep voltammetry curves of $WO_x/g\text{-}C_3N_4$ were tested with Cu^{2+} and U(VI) (Fig. 7f), which was clear that the reduction potential of Cu^{2+} (−0.325 V) was lower than that of U(VI) (−0.394 V). Therefore, the photogenerated electrons were more easily captured by Cu^{2+}, leading to the photoreduction of Cu^{2+} before U(VI). All these experiments above proved its great potential for practical U(VI) removal.

3.4. Possible photocatalytic mechanism

It is well known that both photoreduction of U(VI) and photocatalytic selective oxidation of BA are triggered by radicals, including •OH, $•O_2^-$, photogenerated electron (e^-) and photogenerated hole (h^+). In order to reveal the predominant active ingredient of the photocatalytic reaction on $WO_x/g\text{-}C_3N_4$, room temperature ESR analysis were employed to detect the free radicals generated in the photocatalytic reaction (Figs. 6e and 6f). The typical signal of DMPO-$•O_2^-$ could be clearly observed (Fig. 6e), revealing the presence of $•O_2^-$. However, the signal of DMPO-•OH was not detected (Fig. 6f), indicating the absence of •OH. Moreover, since numbers reports claimed that the benzyl alcohol carbon-centered radical was a crucial reaction intermediate during selective oxidation of BA [20,60], the whole reaction process was traced by ESR. Unsurprisingly, the characteristic peak of the carbon-centered radical appeared in the ESR spectrum (Fig. 8a).

Additionally, to further clarify the specific details and infer the reaction mechanism of the photocatalytic reaction, control experiments were performed through the addition of diverse radical scavengers. In this work, IPA, P-BQ, $KBrO_3$ and TEOA were added as •OH, $•O_2^-$, e^- and h^+ trapping agents, respectively. As seen from Figs. 8b and 8c, the addition of IPA had little effect on the elimination of U(VI) and the conversion of BA, which coincided exactly with the result of the ESR analysis (Fig. 6f). However, the introduction of P-BQ significantly inhibited the conversion of BA and the photoreduction of U(VI). Moreover, in the existence of P-BQ, the conversion percent of BA decreased

more than the elimination ratio of U(VI). Similar changes were also seen in the reaction system with the addition of $KBrO_3$, i.e., the addition of $KBrO_3$ leaded to a decrease in the elimination ratio of U(VI) and the conversion rate of BA, but the elimination ratio of U(VI) decreased more. Those above revealed that $•O_2^-$, e^- and h^+ played crucial roles in the photocatalytic reaction process. Unexpectedly, both the photoreduction of U(VI) and the conversion of BA decreased obviously after adding TEOA. In theory, the quenching of holes by TEOA would limit the oxidation of BA while encouraging the separation of photogenerated e^--h^+ pairs, which would definitely speed up the photoreduction of U(VI). And the above factual results were inconsistent with the theory, indicating that when h^+ was not captured, oxygen did not compete with U(VI) for photogenerated electrons, but combined with the electrons generated by h^+-activated BA. And when h^+ is captured, the electrons generated by h^+-activated BA is not present anymore and oxygen turns around and competes with U(VI) for photogenerated electrons [15]. Thus, the photoreduction rate of U(VI) also decreased. Notably, radical quenching experiments showed the following magnitude of effects on the photoreduction rate of U(VI): $KBrO_3 >$ TEOA > P-BQ, while the effects on the conversion of BA were in the following order: TEOA > P-BQ > $KBrO_3$. In summary, the results suggested that e^- and $•O_2^-$ were directly involved in the reduction of U(VI), while h^+ and $•O_2^-$ were directly engaged in selective oxidation process of BA.

According to the preceding experiments and discussions, a plausible mechanism in this reaction system has been proposed in Scheme 1. Under illumination, the e^--h^+ pairs were produced on $WO_x/g\text{-}C_3N_4$. Meanwhile, the oxygen vacancies would effectively adsorb O_2 and BA. For the oxidation end of the reaction, h^+ activated the BA, resulting in the generation of benzyl alcohol carbon-centered radical and the release of H^+ and e^-. Afterwards, in the presence of a moderate amount of oxygen, the electrons released by the activation of BA rapidly combined with the O_2 adsorbed at oxygen vacancies, generating more reactive $•O_2^-$ radicals. Eventually, $•O_2^-$ further selectively oxidized BA to BD [61,62]. For the reduction end of the reaction, photogenerated electrons directly engaged in the photoreduction of uranyl. If there was too much O_2, O_2 would bound to the electrons released from the activated BA and also to the reducing end to constitute $•O_2^-$ radicals. Finally, the $•O_2^-$ was engaged in the oxidation of benzyl alcohol and the reduction of U(VI). Accordingly, the specific reaction equations could be stated as follows:
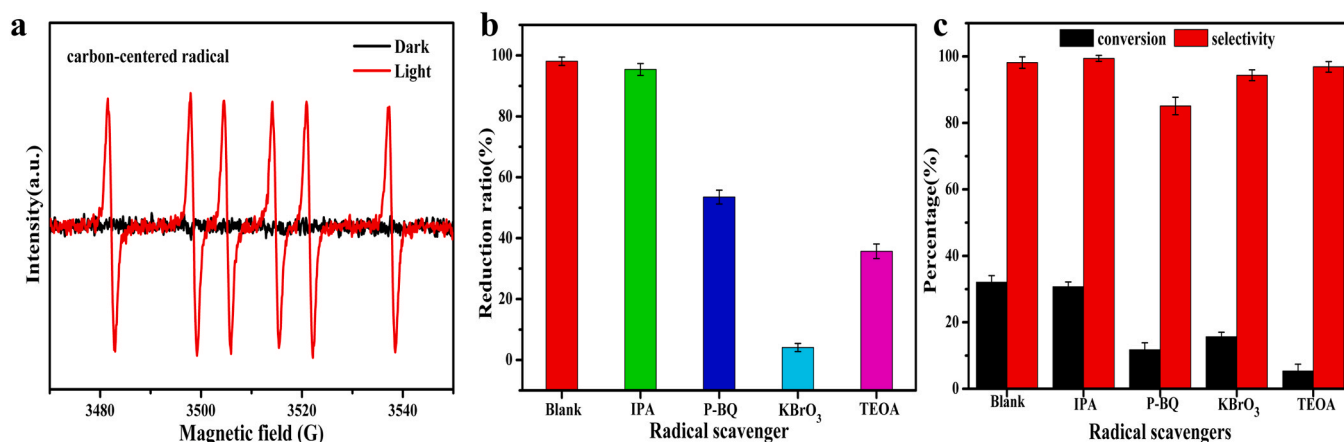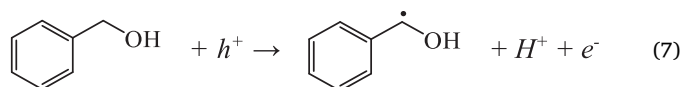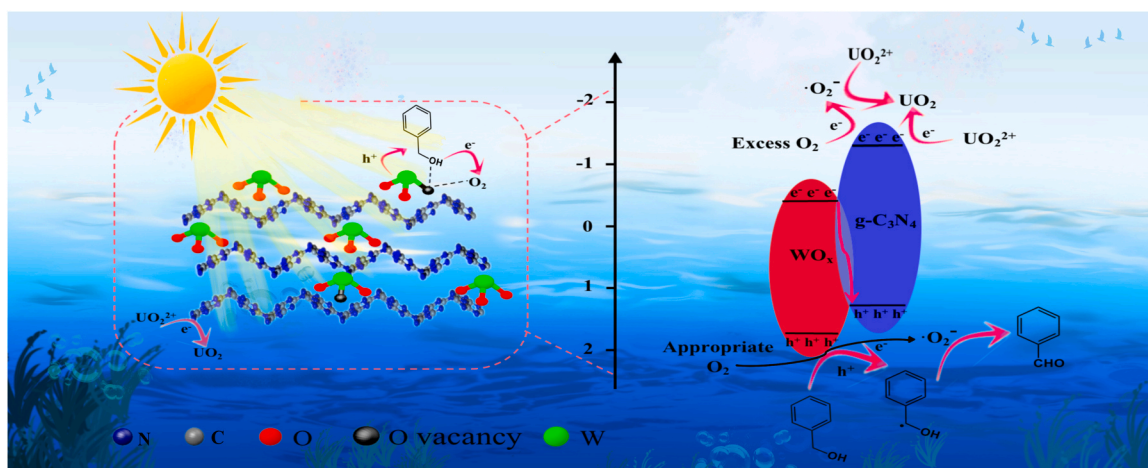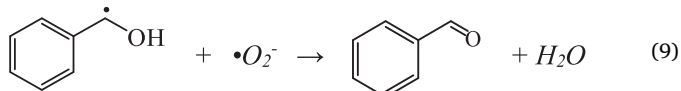
$$WO_x/g\text{-}C_3N_4 + hv \rightarrow e^- + h^+ \tag{5}$$

$$UO_2^{2+} + 2e^- \rightarrow UO_2 \tag{6}$$

$$\text{PhCH}_2\text{OH} + h^+ \rightarrow \text{PhĊHOH} + H^+ + e^- \tag{7}$$

Fig. 8. ESR spectrum of carbon-centered radicals generated in situ (a); Controlled experiments on the photocatalytic performance of $WO_x/g\text{-}C_3N_4$ with different radical scavengers: the photoreduction experiments of U(VI) (b), the selective oxidization experiments of BA (c).

Scheme 1. Possible mechanism of photocatalytic reaction over WO_x/g-C_3N_4.

$$e^- + O_2 \rightarrow \bullet O_2 \qquad (8)$$

$$+ \bullet O_2^- \rightarrow \qquad + H_2O \qquad (9)$$

$$UO_2^{2+} + \bullet O_2^- \rightarrow UO_2 \qquad (10)$$

4. Conclusions

A new WO_x/g-C_3N_4 heterojunction has been prepared through depositing oxygen deficient WO_3 nanosheets on g-C_3N_4. Besides, the WO_x/g-C_3N_4 could effectively photocatalyze the reduction of uranyl and the selective oxidation of BA to BD simultaneously by visible light irradiation in aerobic environment. Compared with bare g-C_3N_4 and single WO_3, the photoreduction activity of WO_x/g-C_3N_4 was 10.4 and 7 times higher, respectively. More importantly, WO_x/g-C_3N_4 performed better than WO_3/g-C_3N_4 in terms of photocatalytic reduction of uranyl (98.5%) and the oxidation selectivity for BA (98.1%) in air atmosphere. And it turned out that the introduction of oxygen vacancies modulated the band gap structure, prevented the formation of strongly oxidizing $\bullet$OH radicals, enhanced the adsorption as well as activation of O_2, and promoted the selective oxidation of BA while accelerating the reduction of U(VI). Notably, since the defect engineering design fixed the right amount of oxygen at the oxidation side, a right amount of O_2 facilitated the synergistic U(VI) reduction and the selective conversion of BA to BD, while an excessive amount of O_2 would battle with U(VI) for photo-generated electrons, thereby inhibiting the reduction of uranyl. And the results also showed that it was feasible to fix oxygen at the oxidation end of the system as a participant of the oxidation reaction by a reasonable structural design. In addition, WO_x/g-C_3N_4 exhibited excellent anti-interference ability and cyclic stability for the photoreduction of uranyl. Finally, a new mechanism has been proposed. This study not only effectively overcomes the effect of O_2 in the U(VI) reduction process, but also effectively uses the h^+ and oxygen at the oxidation end to prepare high-value chemicals at the same time. More importantly this will help to construct catalysts with higher activity for synergistic reduction and oxidation under aerobic conditions.

CRediT authorship contribution statement

Feng He devised experiments, conducted experiments, collected the data and processed it, and wrote the manuscript; **Qianxiang Xiao**

simulated the DFT calculations and helped to revise the manuscript; **Yin Chen** prepared the materials, conducted experiments; **Hongqing Wang** and **Xiangke Wang** conceived the project, discussion and revised the manuscript.

Declaration of Competing Interest

The authors declare that they have no known competing financial interests or personal relationships that could have appeared to influence the work reported in this paper.

Data availability

Data will be made available on request.

Appendix A. Supporting information

Supplementary data associated with this article can be found in the online version at doi:10.1016/j.apcatb.2023.123525.

References

[1] Z.H. Zhang, J.H. Lan, L.Y. Yuan, P.P. Sheng, M.Y. He, L.R. Zheng, Q. Chen, Z. F. Chai, J.K. Gibson, W.Q. Shi, Rational construction of porous metal–organic frameworks for uranium(VI) extraction: the strong periodic tendency with a metal node, ACS Appl. Mater. Interfaces 12 (2020) 14087–14094, https://doi.org/10.1021/acsami.0c02121.

[2] Y. Liu, Z. Zhao, D. Yuan, Y. Wang, Y. Dai, Y. Zhu, J.W. Chew, Introduction of amino groups into polyphosphazene framework supported on CNT and coated Fe_3O_4 nanoparticles for enhanced selective U(VI) adsorption, Appl. Surf. Sci. 466 (2019) 893–902, https://doi.org/10.1016/j.apsusc.2018.10.097.

[3] K. Yu, P. Jiang, H. Yuan, R. He, W. Zhu, L. Wang, Cu-based nanocrystals on ZnO for uranium photoreduction: plasmon-assisted activity and entropy-driven stability, Appl. Catal. B-Environ. 288 (2021), https://doi.org/10.1016/j.apcatb.2021.119978.

[4] C. Dong, T. Qiao, Y. Huang, X. Yuan, J. Lian, T. Duan, W. Zhu, R. He, Efficient photocatalytic extraction of uranium over ethylenediamine capped cadmium sulfide telluride nanobelts, ACS Appl. Mater. Interfaces 13 (2021) 11968–11976, https://doi.org/10.1021/acsami.0c22800.

[5] F. Yu, Z. Zhu, S. Wang, Y. Peng, Z. Xu, Y. Tao, J. Xiong, Q. Fan, F. Luo, Tunable perylene-based donor-acceptor conjugated microporous polymer to significantly enhance photocatalytic uranium extraction from seawater, Chem. Eng. J. 412 (2021), https://doi.org/10.1016/j.cej.2020.127558.

[6] D.S. Selishchev, T.N. Filippov, M.N. Lyulyukin, D.V. Kozlov, Uranyl-modified TiO_2 for complete photocatalytic oxidation of volatile organic compounds under UV and

visible light, Chem. Eng. J. 370 (2019) 1440–1449, https://doi.org/10.1016/j.cej.2019.03.280.

[7] H. Wang, H. Guo, N. Zhang, Z. Chen, B. Hu, X. Wang, Enhanced photoreduction of U(VI) on C_3N_4 by Cr(VI) and Bisphenol A: ESR, XPS, and EXAFS investigation, Environ. Sci. Technol. 53 (2019) 6454–6461, https://doi.org/10.1021/acs.est.8b06913.

[8] C. Lu, R. Chen, X. Wu, M. Fan, Y. Liu, Z. Le, S. Jiang, S. Song, Boron doped g-C_3N_4 with enhanced photocatalytic UO_2^{2+} reduction performance, Appl. Surf. Sci. 360 (2016) 1016–1022, https://doi.org/10.1016/j.apsusc.2015.11.112.

[9] X. Liu, R.-X. Bi, C.-R. Zhang, Q.X. Luo, R.P. Liang, J.D. Qiu, SnS_2-covalent organic framework Z-scheme van der Waals heterojunction for enhanced photocatalytic reduction of uranium (VI) in rare earth tailings wastewater, Chem. Eng. J. 460 (2023), https://doi.org/10.1016/j.cej.2023.141756.

[10] S. Bai, N. Zhang, C. Gao, Y. Xiong, Defect engineering in photocatalytic materials, Nano Energy 53 (2018) 296–336, https://doi.org/10.1016/j.nanoen.2018.08.058.

[11] P.L. Liang, L.Y. Yuan, H. Deng, X.C. Wang, L. Wang, Z.J. Li, S.Z. Luo, W.Q. Shi, Photocatalytic reduction of uranium(VI) by magnetic $ZnFe_2O_4$ under visible light, Appl. Catal. B-Environ. 267 (2020), https://doi.org/10.1016/j.apcatb.2020.118688.

[12] P. Li, J. Wang, Y. Wang, J. Liang, D. Pan, S. Qiang, Q. Fan, An overview and recent progress in the heterogeneous photocatalytic reduction of U(VI), J. Photochem. Photobiol. C. -Photochem. Rev. 41 (2019), https://doi.org/10.1016/j.jphotochemrev.2019.100320.

[13] X. Wu, S. Jiang, S. Song, C. Sun, Constructing effective photocatalytic purification system with P-introduced g-C_3N_4 for elimination of UO_2^{2+}, Appl. Surf. Sci. 430 (2018) 371–379, https://doi.org/10.1016/j.apsusc.2017.06.065.

[14] Z. Le, C. Xiong, J. Gong, X. Wu, T. Pan, Z. Chen, Z. Xie, Self-cleaning isotype g-C_3N_4 heterojunction for efficient photocatalytic reduction of hexavalent uranium under visible light, Environ. Pollut. 260 (2020), https://doi.org/10.1016/j.envpol.2020.114070.

[15] Y. Li, L. Shi, Y. Mao, Y. Zhang, H. Wang, Efficient reduction of uranyl under aerobic conditions by sodium and potassium co-doped carbon nitride, Chem. Eng. J. 446 (2022), https://doi.org/10.1016/j.cej.2022.136872.

[16] Y. Zhang, M. Zhu, S. Zhang, Y. Cai, Z. Lv, M. Fang, X. Tan, X. Wang, Highly efficient removal of U(VI) by the photoreduction of $SnO_2/CdCO_3/CdS$ nanocomposite under visible light irradiation, Appl. Catal. B-Environ. 279 (2020), https://doi.org/10.1016/j.apcatb.2020.119390.

[17] Z. Li, Z. Zhang, X. Zhu, C. Meng, Z. Dong, S. Xiao, Y. Wang, Y. Wang, X. Cao, Y. Liu, Exciton dissociation and transfer behavior and surface reaction mechanism in Donor–Acceptor organic semiconductor photocatalytic separation of uranium, Appl. Catal. B-Environ. 332 (2023), https://doi.org/10.1016/j.apcatb.2023.122751.

[18] N. Liu, R. Li, J. Zhu, Q. Liu, R. Chen, J. Yu, Y. Li, H. Zhang, J. Wang, Z-scheme heterojunction ZnS/WO_3 composite: photocatalytic reduction of uranium and band gap regulation mechanism, J. Colloid Interface Sci. 630 (2023) 727–737, https://doi.org/10.1016/j.jcis.2022.10.151.

[19] S. Jiang, C. Li, Y. Muhammad, Y. Tang, R. Wang, J. Li, J. Li, Z. Zhao, Z. Zhao, Solvent-induced fabrication of Cu/MnO_x nanosheets with abundant oxygen vacancies for efficient and long-lasting photothermal catalytic degradation of humid toluene vapor, Appl. Catal. B-Environ. 328 (2023), https://doi.org/10.1016/j.apcatb.2023.122509.

[20] H. Li, F. Qin, Z. Yang, X. Cui, J. Wang, L. Zhang, New reaction pathway induced by plasmon for selective benzyl alcohol oxidation on BiOCl possessing oxygen vacancies, J. Am. Chem. Soc. 139 (2017) 3513–3521, https://doi.org/10.1021/jacs.6b12850.

[21] Y. Zhang, Q. Chen, Q. Xiao, L. Shi, Z. Zhao, H. Wang, Enhancement of CdS resistance to photocorrosion and photocatalytic removal of uranyl by complexation with N-deficient g-C_3N_4 under aerobic conditions, Chemosphere 335 (2023), https://doi.org/10.1016/j.chemosphere.2023.139022.

[22] Y.H. Chew, J.Y. Tang, L.J. Tan, B.W.J. Choi, L.L. Tan, S.P. Chai, Engineering surface oxygen defects on tungsten oxide to boost photocatalytic oxygen evolution from water splitting, Chem. Commun. 55 (2019) 6265–6268, https://doi.org/10.1039/c9cc01449g.

[23] J. Lei, H. Liu, C. Yuan, Q. Chen, J.A. Liu, F. Wen, X. Jiang, W. Deng, X. Cui, T. Duan, W. Zhu, R. He, Enhanced photoreduction of U(VI) on WO_3 nanosheets by oxygen defect engineering, Chem. Eng. J. 416 (2021), https://doi.org/10.1016/j.cej.2021.129164.

[24] S.J. Shah, W. Li, Y. Tang, Y. Hu, S. Jiang, H. He, R. Wang, Z. Zhao, Z. Zhao, Ligand-sharing growth of upconversion UCNP(NaYbF$_4$:Tm^{3+})/NMIL(Ti) nanohybrids with extended light absorbance for acetaldehyde photodegradation under high humidity, Appl. Catal. B-Environ. 315 (2022), https://doi.org/10.1016/j.apcatb.2022.121555.

[25] W.J. Ong, L.L. Tan, Y.H. Ng, S.T. Yong, S.P. Chai, Graphitic carbon nitride (g-C_3N_4)-based photocatalysts for artificial photosynthesis and environmental remediation: are we a step closer to achieving sustainability? Chem. Rev. 116 (2016) 7159–7329, https://doi.org/10.1021/acs.chemrev.6b00075.

[26] L. Hu, Z. Ding, F. Yan, Y.M. Du, Q. Xiao, H. Wang, Inhibition of superoxide radical diffusion by Van der Waals forces for boosting photocatalytic H_2O_2 production, Appl. Surf. Sci. 638 (2023), https://doi.org/10.1016/j.apsusc.2023.158135.

[27] X. Wang, K. Maeda, A. Thomas, K. Takanabe, G. Xin, J.M. Carlsson, K. Domen, M. Antonietti, A metal-free polymeric photocatalyst for hydrogen production from water under visible light, Nat. Mater. 8 (2009) 76–80, https://doi.org/10.1038/nmat2317.

[28] X.H. Jiang, Q.J. Xing, X.B. Luo, F. Li, J.P. Zou, S.-S. Liu, X. Li, X.K. Wang, Simultaneous photoreduction of Uranium(VI) and photooxidation of Arsenic(III) in aqueous solution over g-C_3N_4/TiO_2 heterostructured catalysts under simulated

[29] T. Xiao, Z. Tang, Y. Yang, L. Tang, Y. Zhou, Z. Zou, In situ construction of hierarchical WO_3/g-C_3N_4 composite hollow microspheres as a Z-scheme photocatalyst for the degradation of antibiotics, Appl. Catal. B-Environ. 220 (2018) 417–428, https://doi.org/10.1016/j.apcatb.2017.08.070.

[30] Z. Wang, Z. Wang, X. Zhu, C. Ai, Y. Zeng, W. Shi, X. Wang, H. Zhang, H. Si, J. Li, C. Z. Wang, S. Lin, Photodepositing CdS on the active cyano groups decorated g-C_3N_4 in Z-scheme manner promotes visible-light-driven hydrogen evolution, Small 17 (2021), e2102699, https://doi.org/10.1002/smll.202102699.

[31] S. Yang, Q. Li, L. Chen, Z. Chen, B. Hu, H. Wang, X. Wang, Synergistic removal and reduction of U(VI) and Cr(VI) by Fe_3S_4 micro-crystal, Chem. Eng. J. 385 (2020), https://doi.org/10.1016/j.cej.2019.123909.

[32] G. Kresse, J. Hafner, Ab initio molecular dynamics for liquid metals, Phys. Rev. B 47 (1993) 558–561, https://doi.org/10.1103/physrevb.47.558.

[33] G. Kresse, J. Furthmüller, Efficiency of ab-initio total energy calculations for metals and semiconductors using a plane-wave basis set, Comput. Mater. Sci. 6 (1996) 15–50, https://doi.org/10.1016/0927-0256(96)00008-0.

[34] J.P. Perdew, Y. Wang, Accurate and simple analytic representation of the electron-gas correlation energy, Phys. Rev. B-Condens Matter 45 (1992) 13244–13249, https://doi.org/10.1103/physrevb.45.13244.

[35] J.P. Perdew, K. Burke, M. Ernzerhof, Generalized gradient approximation made simple, Phys. Rev. Lett. 77 (18) (1996) 3865–3868, https://doi.org/10.1103/PhysRevLett.77.3865.

[36] P.E. Blöchl, Projector augmented-wave method, Phys. Rev. B 50 (1994) 17953, https://doi.org/10.1103/PhysRevB.50.17953.

[37] S. Grimme, S. Ehrlich, L. Goerigk, Effect of the damping function in dispersion corrected density functional theory, J. Comput. Chem. 32 (2011) 1456–1465, https://doi.org/10.1002/jcc.21759.

[38] S. Grimme, J. Antony, S. Ehrlich, H. Krieg, A consistent and accurate ab initio parametrization of density functional dispersion correction (DFT-D) for the 94 elements H-Pu, J. Chem. Phys. 132 (2010), 154104, https://doi.org/10.1063/1.3382344.

[39] C.J. Howard, V. Luca, K.S. Knight, High-temperature phase transitions in tungsten trioxide-the last word? J. Phys. -Condes. Matter 14 (2002) 377–387, https://doi.org/10.1088/0953-8984/14/3/308.

[40] M.J. Bojdys, J.-O. Müller, M. Antonietti, A. Thomas, Ionothermal synthesis of crystalline, condensed, graphitic carbon nitride, Chem. -Eur. J. 14 (2008) 8177–8182, https://doi.org/10.1002/chem.200800190.

[41] V. Wang, N. Xu, J.C. Liu, G. Tang, W.-T. Geng, VASPKIT: a user-friendly interface facilitating high-throughput computing and analysis using VASP code, Comput. Phys. Commun. 267 (2021), https://doi.org/10.1016/j.cpc.2021.108033.

[42] N. Zhang, X. Li, H. Ye, S. Chen, H. Ju, D. Liu, Y. Lin, W. Ye, C. Wang, Q. Xu, J. Zhu, L. Song, J. Jiang, Y. Xiong, Oxide defect engineering enables to couple solar energy into oxygen activation, J. Am. Chem. Soc. 138 (2016) 8928–8935, https://doi.org/10.1021/jacs.6b04629.

[43] C. Li, Y. Du, D. Wang, S. Yin, W. Tu, Z. Chen, M. Kraft, G. Chen, R. Xu, Unique P-Co-N surface bonding states constructed on g-C_3N_4 nanosheets for drastically enhanced photocatalytic Activity of H_2 evolution, Adv. Funct. Mater. 27 (2017), https://doi.org/10.1002/adfm.201604328.

[44] X. Zhan, H. Wang, G. Zhou, L. Chen, Y. Sun, Y. Zhao, J. Liu, H. Shi, Uracil-doped graphitic carbon nitride for enhanced photocatalytic performance, ACS Appl. Mater. Interfaces 13 (2021) 12118–12130, https://doi.org/10.1021/acsami.1c00771.

[45] J. Fu, Q. Xu, J. Low, C. Jiang, J. Yu, Ultrathin 2D/2D WO_3/g-C_3N_4 step-scheme H_2-production photocatalyst, Appl. Catal. B-Environ. 243 (2019) 556–565, https://doi.org/10.1016/j.apcatb.2018.11.011.

[46] S. Zhou, Y. Liu, J. Li, Y. Wang, G. Jiang, Z. Zhao, D. Wang, A. Duan, J. Liu, Y. Wei, Facile in situ synthesis of graphitic carbon nitride (g-C_3N_4)-N-TiO_2 heterojunction as an efficient photocatalyst for the selective photoreduction of CO_2 to CO, Appl. Catal. B-Environ. 158–159 (2014) 20–29, https://doi.org/10.1016/j.apcatb.2014.03.037.

[47] X.Y. Zhang, J.J. Wang, P. Li, Z.Y. Tan, J.H. Zeng, Y.R. He, N. Habibul, Removal of U (VI) from aqueous solution via photocatalytic reduction over WO_3/g-C_3N_4 composite under visible light, Chem. Eng. J. 428 (2022), https://doi.org/10.1016/j.cej.2021.131209.

[48] Z. Dai, Z. Lian, Y. Sun, L. Li, H. Zhang, N. Hu, D. Ding, Fabrication of g-C_3N_4/Sn_3O_4/Ni electrode for highly efficient photoelectrocatalytic reduction of U(VI), Chem. Eng. J. 433 (2022), https://doi.org/10.1016/j.cej.2021.133766.

[49] S. Wei, H. Zhong, H. Wang, Y. Song, C. Jia, M. Anpo, L. Wu, Oxygen vacancy enhanced visible light photocatalytic selective oxidation of benzylamine over ultrathin Pd/BiOCl nanosheets, Appl. Catal. B-Environ. 305 (2022), https://doi.org/10.1016/j.apcatb.2021.121032.

[50] J.Y. Tang, R.T. Guo, W.G. Zhou, C.Y. Huang, W.G. Pan, Ball-flower like NiO/g-C_3N_4 heterojunction for efficient visible light photocatalytic CO_2 reduction, Appl. Catal. B-Environ. 237 (2018) 802–810, https://doi.org/10.1016/j.apcatb.2018.06.042.

[51] A. Yuan, H. Lei, Z. Wang, X. Dong, Improved photocatalytic performance for selective oxidation of amines to imines on graphitic carbon nitride/bismuth tungstate heterojunctions, J. Colloid Interface Sci. 560 (2020) 40–49, https://doi.org/10.1016/j.jcis.2019.10.060.

[52] S. Sun, R. Gao, X. Liu, L. Pan, C. Shi, Z. Jiang, X. Zhang, J.J. Zou, Engineering interfacial band bending over bismuth vanadate/carbon nitride by work function regulation for efficient solar-driven water splitting, Sci. Bull. 67 (2022) 389–397, https://doi.org/10.1016/j.scib.2021.10.009.

[53] N. Chen, Y. Zhou, S. Cao, R. Wang, W. Jiao, A novel strategy for loading metal cocatalysts onto hollow nano-TiO_2 inner surface with highly enhanced H_2

production activity, Green. Energy Environ. 8 (2023) 509–518, https://doi.org/10.1016/j.gee.2021.07.002.

[54] X. Sun, X. Luo, X. Zhang, J. Xie, S. Jin, H. Wang, X. Zheng, X. Wu, Y. Xie, Enhanced superoxide generation on defective surfaces for selective photooxidation, J. Am. Chem. Soc. 141 (2019) 3797–3801, https://doi.org/10.1021/jacs.8b13051.

[55] X. Xiao, J. Jiang, L. Zhang, Selective oxidation of benzyl alcohol into benzaldehyde over semiconductors under visible light: The case of $Bi_{12}O_{17}Cl_2$ nanobelts, Appl. Catal. B-Environ. 142–143 (2013) 487–493, https://doi.org/10.1016/j.apcatb.2013.05.047.

[56] F. Su, S.C. Mathew, G. Lipner, X. Fu, M. Antonietti, S. Blechert, X. Wang, mpg-C_3N_4-Catalyzed selective oxidation of alcohols using O_2 and visible light, J. Am. Chem. Soc. 132 (2010) 16299–16301, https://doi.org/10.1021/ja102866p.

[57] X. Rong, H. Chen, J. Rong, X. Zhang, J. Wei, S. Liu, X. Zhou, J. Xu, F. Qiu, Z. Wu, An all-solid-state Z-scheme TiO_2/$ZnFe_2O_4$ photocatalytic system for the N_2 photofixation enhancement, Chem. Eng. J. 371 (2019) 286–293, https://doi.org/10.1016/j.cej.2019.04.052.

[58] C. Zhang, Y. Liu, X. Li, H. Chen, T. Wen, Z. Jiang, Y. Ai, Y. Sun, T. Hayat, X. Wang, Highly uranium elimination by crab shells-derived porous graphitic carbon nitride:

batch, EXAFS and theoretical calculations, Chem. Eng. J. 346 (2018) 406–415, https://doi.org/10.1016/j.cej.2018.03.186.

[59] X. Wu, Y. Mao, D. Wang, Q. Huang, Q. Yin, M. Zheng, Q. Hu, H. Wang, Designing a colorimetric sensor containing nitrogen and oxygen atoms for uranyl ions identification: chromatic mechanism, binding feature and on-site application, Sens. Actuator B-Chem. 307 (2020), https://doi.org/10.1016/j.snb.2020.127681.

[60] L. Luo, Z.J. Wang, X. Xiang, D. Yan, J. Ye, Selective activation of benzyl alcohol coupled with photoelectrochemical water oxidation via a radical relay strategy, ACS Catal. 10 (2020) 4906–4913, https://doi.org/10.1021/acscatal.0c00660.

[61] Y. Keum, S. Park, Y.P. Chen, J. Park, Titanium-carboxylate metal-organic framework based on an unprecedented Ti-Oxo chain cluster, Angew. Chem. -Int. Ed. 57 (2018) 14852–14856, https://doi.org/10.1002/anie.201809762.

[62] Z. Zhou, Y.-N. Xie, W. Zhu, H. Zhao, N. Yang, G. Zhao, Selective photoelectrocatalytic tuning of benzyl alcohol to benzaldehyde for enhanced hydrogen production, Appl. Catal. B-Environ. 286 (2021), https://doi.org/10.1016/j.apcatb.2020.119868.